Supplementary Material

1 DATA

The data is available from 10.3929/ethz-b-000339583

2 BEDROCK DEM

The Bedrock DEM of Gauligletscher was reconstructed from Ground Penetrating Radar (GPR) profiles (Rutishauser et al., 2016). To complete the data where the profile density was to low, we used the ice thickness distribution approach of Farinotti et al. (2009), see Fig. S1. The ice thickness distribution was obtained by subtracting the bedrock DEM from the surface DEM, representing a consistent state of 2010.

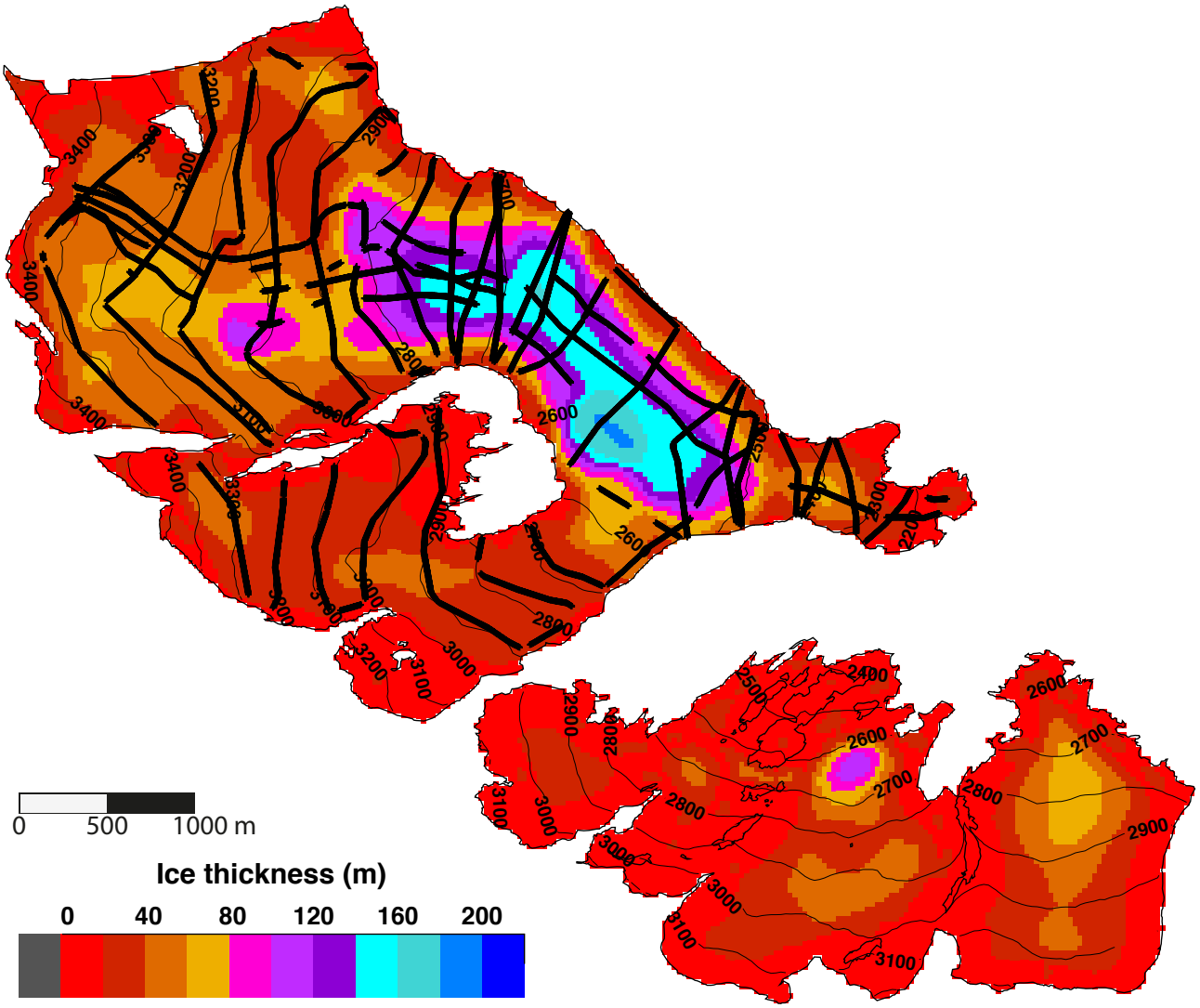

Figure S1. Ice thickness distribution of Gauligletscher and Grünbergligletscher in 2010. The thick black lines are the locations where the bedrock was identified by GPR.

3 MODEL CALIBRATION

Table S1 shows several assessment results of the model quality with respect to ice flow parameters (rate factor A and Weertman friction coefficient c). The first consists of the Root Mean Square Error (RMSE) between modelled and observed surface elevation in 2010. The second and third consist of the RMSE between modelled and observed surface velocities (TanDEM-X and Sentinel-2). The fourth shows the modelled depth of the pieces of the airplane in 1947 obtained after integrating backward-in-time their trajectories from the location they were found. The first three panels were used for model calibration, i.e., the ice flow parameters were chosen in order to minimize discrepancy. Furthermore, the spatial distribution of the RMSE is shown on Figure S2 for the optimal parameter set $(A, c) = (60\ \text{MPa}^{-3}\ \text{a}^{-1}, 12500\ \text{MPa}^{-3}\ \text{m a}^{-1})$.

Table S1. The three first panels indicate the Root Mean Square Error (RMSE) between modelled surface elevation and the DEM of 2010 (m), between modelled surface velocities and those inferred from SAR data of TanDEM-x (m a^{-1}), and from Sentinel-2 in the ablation area (m a^{-1}), respectively, for different combinations of model parameters A (MPa^{-3} a^{-1}) and c (MPa^{-3} m a^{-1}). The bottom panel shows the modelled depth of the pieces of the airplane in 1947 obtained after integrating backward-in-time their trajectories from the location they were found.

	Weertman (c)	Rate factor (A)				
		60	80	100	120	150
DEM 2010	57'900	26.9	27.5	28.1	28.6	29.2
	37'000	21.9	22.6	23.3	23.9	24.6
	23'300	17.4	18.1	18.7	19.4	20.3
	12'500	13.8	14.2	14.7	15.2	16.0
	0	29.1	23.6	20.1	18.0	16.1
TanDEM-X	57'900	36.3	39.6	42.4	44.8	48.3
	37'000	23.9	26.2	28.2	30.2	33.0
	23'300	15.6	17.1	18.6	20.2	22.0
	12'500	11.4	11.8	12.4	13.1	14.4
	0	15.5	14.6	13.9	13.3	12.6
Sentinel-2	57'900	44.5	49.4	53.3	56.9	62.2
	37'000	29.7	33.3	36.5	39.6	44.0
	23'300	18.5	21.4	24.1	26.9	30.0
	12'500	9.8	11.5	13.7	15.4	18.5
	0	10.6	9.2	8.1	7.5	7.5
Emerged pc.	57'900	22.5	32.7	31.9	31.8	33.5
	37'900	24.6	25.6	25.4	27.5	35.1
	23'300	42.4	42.3	37.1	32.0	28.1
	12'500	68.9	43.3	34.8	43.5	44.0
	0	138.8	122.7	114.8	108.3	100.8

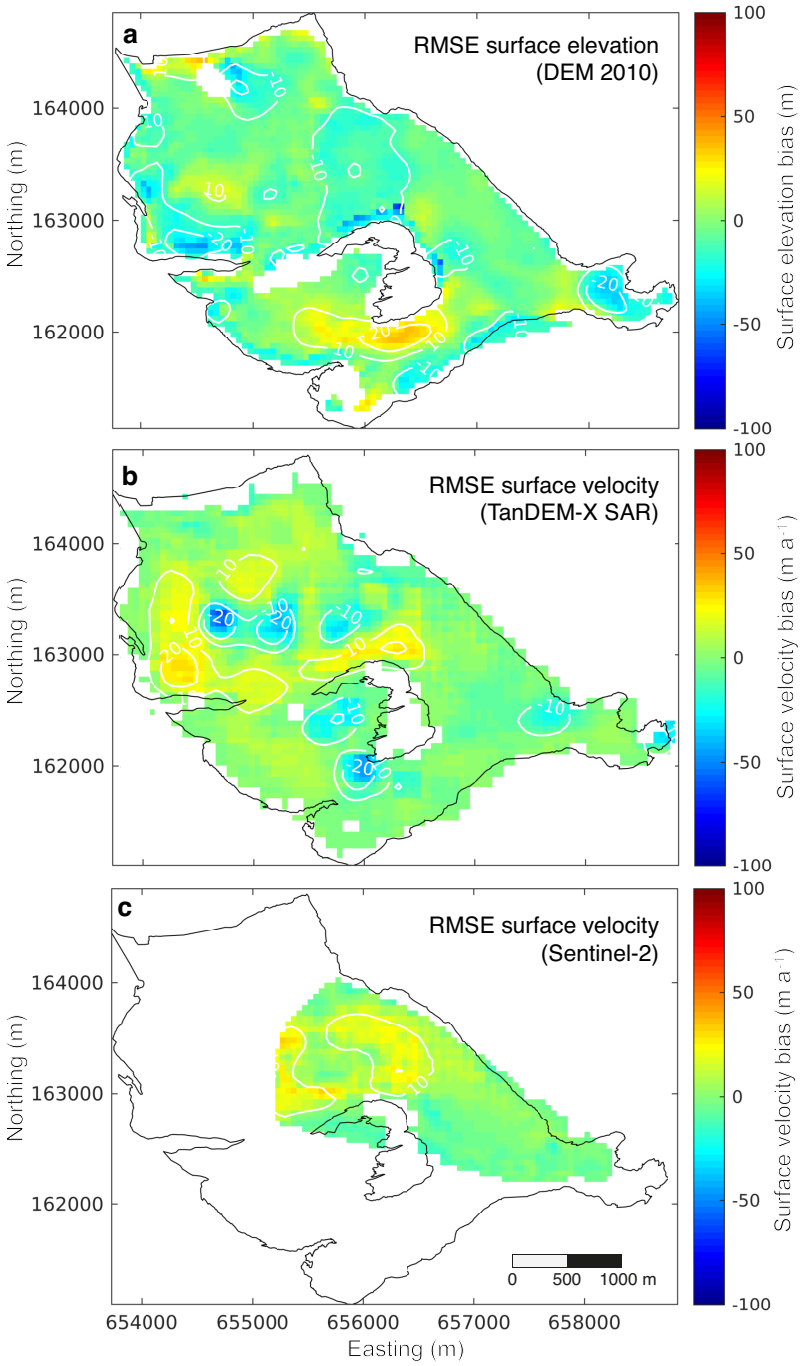

Figure S2. Root Mean Square Error (RMSE) between modelled and observed (a) surface elevation in 2010, (b) averaged surface velocity between 2011 and 2016 using TanDEM-X SAR data and (c) averaged surface velocity between 2015 and 2017 using the Sentinel-2 data. Negative difference means that the modelled surface/velocity is too low/slow and positive difference means it is too high/fast compared to observations.

4 MODELLED MASS BALANCE IN 2011 AND 2013

Figure S3 displays the spatial distribution of the modelled annual mass balance in 2011 and 2013. These two distributions were used to run the model in the future for the warm-dry and cold-wet scenarios, respectively.

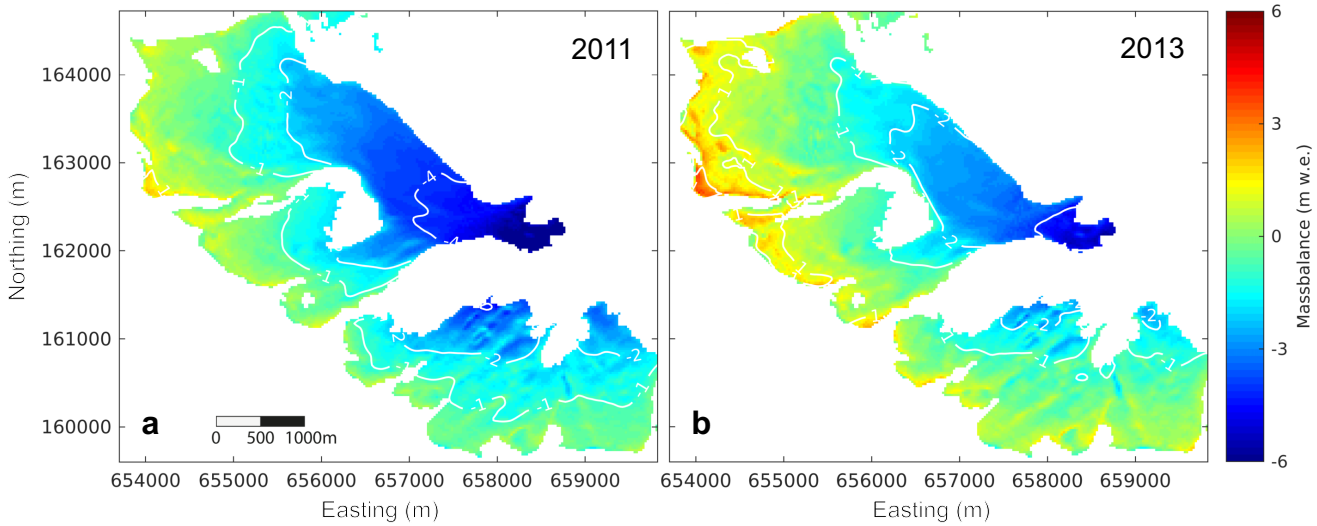

Figure S3. Spatial distribution of the modelled annual mass balance in (a) 2011 and (b) 2013 (unit: m water equivalent). These two mass balance distributions were used for the warm-dry and cold-wet scenarios to simulate the evolution of Gauligletscher in the future.

5 SENSITIVITY OF THE RESULTS

Figure S4 shows the modelled horizontal locations and their confidence areas of the Dakota in 2014, of the Dakota in the year of emergence, and of the already-emerged pieces in 1947. Taking into account all sources of uncertainty listed in Section 5.3, the confidence areas are 1012, 954, 949 m long and 67, 119, 74 m wide, respectively (see Supplementary Fig. 4).

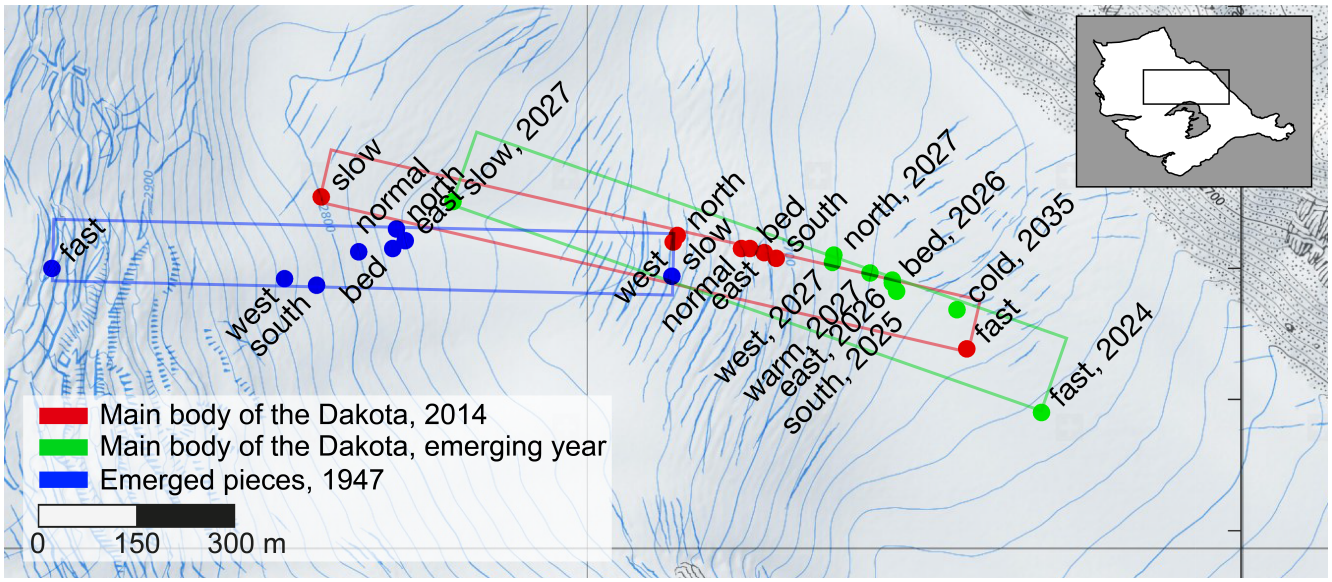

Figure S4. Modelled horizontal position of the Dakota main body in 2014 (red), of the Dakota main body in the emergence year (green), and of the emerged pieces (blue). The rectangle indicates the confidence area, which takes into account model errors and data uncertainties.

6 GPR SEARCH INVESTIGATIONS

In April 2018 we used Ground Penetrating Radar (GPR) to conduct measurements at the surface of Gauligletscher in order to localize the Dakota aircraft, as GPR techniques had previously detecting plane wreckages and buried debris within ice sheets (Annan, 2004; Colgan et al., 2016). To achieve this, electromagnetic waves were propagated from the transmitting antenna, and scattered or reflected within a glacial setting, from bedrock, englacial water accumulations or via materials with different electrical or magnetic proprieties (Plewes and Hubbard, 2001; Conyers, 2002). These reflected radar waves were then detected by the receiving antenna. We attached the pulseEKKO GPR system on two sleds (one for the transmitting and one for the receiving antenna) and acquired 9 km of radar data parallel and perpendicular to the ice flow. The lines were spaced by approximately 40 m intervals, covering a major portion of the Dakota aircraft modelled confidence area in 2018 (Fig. S5a). Two different antenna frequencies (50 MHz and 25 MHz) were used to increase our ability to identify the Dakota aircraft by changing the resulting vertical resolutions. A global navigation satellite system (GNSS) receiver was connected to the GPR recorder to link each radargram trace to a 3D spatial coordinate.

However, in the area and depth range where the Dakota aircraft was estimated to be located by the model, the data were characterized by large scattering features, and no distinct reflections are visible (see an example on Fig. S5b). Such data features are extreme common in temperate condition on alpine glaciers

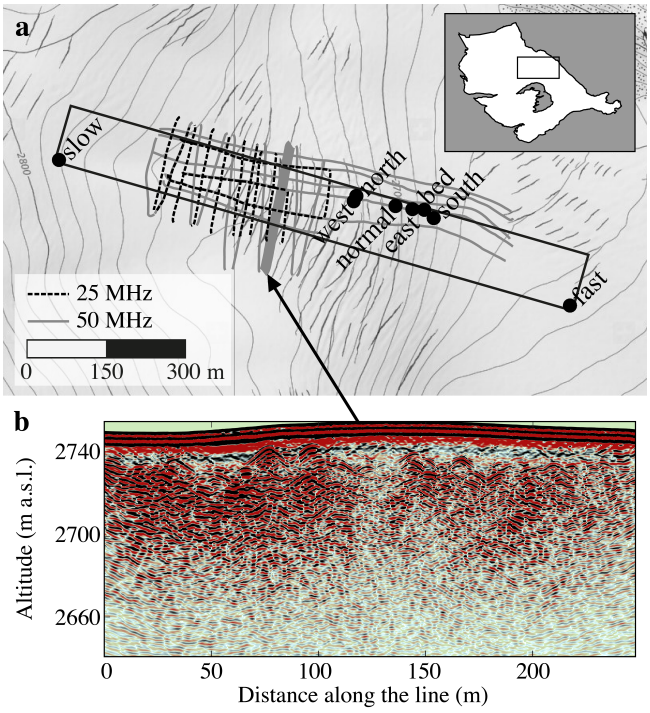

Figure S5. (a) Overview of 25 MHz and 50 MHz profiles performed in April 2018 on Gauligletscher. The black dots represent the modelled horizontal location of the Dakota aircraft in 2018, while the rectangle indicates the coresponding confidence area accounting for various sources of error. (b) GPR profile signal amplitude (intensity of reflection) displayed as a function of distance along the bold grey line shown on Panel a (x-axis) and altitude (y-axis).

(Langhammer et al., 2017). Consequently, we cannot clearly distinguish any reflections caused by the Dakota aircraft. Possible technical reasons are:

1. Gauligletscher is a temperate glacier and the use of GPR could generate erratic results in temperate ice due to water content in the bulk of the ice which may cause damping and scattering of the electromagnetic waves. For this reason, the scattering in the data can likely be traced to surface or shallow englacial water (Fig. S5b) (Maijala et al., 1998; Moore et al., 1999; Langhammer et al., 2017). By contrast, the airplanes in Greenland detected by GPR (see Introduction) were located in cold ice, and thus less affected by wave scattering (Moore et al., 1999).
2. High amplitude point diffraction – the expected feature caused by an obstacle such as the Dakota aircraft – could also originate from englacial voids, sediment inclusions (Irvine-Fynn et al., 2006) or drainage channels (Moorman and Michel, 2000).

Lastly, it cannot be ruled out that the Dakota aircraft could be broken apart into several small pieces, which would generate only sparse and small diffractions, and/or that the wreck could be located outside of the GPR measurement lines.

REFERENCES

Annan, A. (2004). Applications of ground penetrating radar in archaeological and forensic contexts. *First Break* 22, 41–44

Colgan, W., Machguth, H., MacFerrin, M., Colgan, J. D., van As, D., and MacGregor, J. A. (2016). The abandoned ice sheet base at Camp Century, Greenland, in a warming climate: RECONSIDERING CAMP CENTURY. *Geophysical Research Letters* 43, 8091–8096. doi:10.1002/2016GL069688

Conyers, L. B. (2002). Ground Penetrating radar. In *Encyclopedia of Imaging Science and Technology*, ed. J. P. Hornak (Hoboken, NJ, USA: John Wiley & Sons, Inc.). doi:10.1002/0471443395.img026

Farinotti, D., Huss, M., Bauder, A., Funk, M., and Truffer, M. (2009). A method to estimate the ice volume and ice-thickness distribution of alpine glaciers. *Journal of Glaciology* 55, 422–430. doi:10.3189/002214309788816759

Irvine-Fynn, T. D. L., Moorman, B. J., Williams, J. L. M., and Walter, F. S. A. (2006). Seasonal changes in ground-penetrating radar signature observed at a polythermal glacier, Bylot Island, Canada. *Earth Surface Processes and Landforms* 31, 892–909. doi:10.1002/esp.1299

Langhammer, L., Rabenstein, L., Bauder, A., and Maurer, H. (2017). Ground-penetrating radar antenna orientation effects on temperate mountain glaciers. *Geophysics* 82, H15–H24. doi:10.1190/geo2016-0341.1

Maijala, P., Moore, J., Hjelt, S., Pälli, A., and Sinisalo, A. (1998). GPR investigations of glaciers and sea ice in the Scandinavian Arctic. *Proceedings of the 7th International Conference on GPR (GPR'98)* , 143–47

Moore, J., Pälli, A., Ludwig, F., Blatter, H., Jania, J., Gadek, B., et al. (1999). High-resolution hydrothermal structure of Hansbreen, Spitsbergen, mapped by ground-penetrating radar. *Journal of Glaciology* 45, 524–532. doi:10.3189/S0022143000001386

Moorman, B. J. and Michel, F. A. (2000). Glacial hydrological system characterization using ground-penetrating radar. *Hydrological Processes* 14, 2645–2667. doi:10.1002/1099-1085(20001030)14:15⟨2645::AID-HYP84⟩3.0.CO;2-2

Plewes, L. A. and Hubbard, B. (2001). A review of the use of radio-echo sounding in glaciology. *Progress in Physical Geography* 25, 203–236. doi:10.1177/030913330102500203

Rutishauser, A., Maurer, H., and Bauder, A. (2016). Helicopter-borne ground-penetrating radar investigations on temperate alpine glaciers: A comparison of different systems and their abilities for bedrock mapping. *Geophysics* 81, WA119–WA129. doi:10.1190/geo2015-0144.1